nature energy

ARTICLES

PUBLISHED: 19 DECEMBER 2016 | VOLUME: 2 | ARTICLE NUMBER: 16191

Ultrastable low-bias water splitting photoanodes via photocorrosion inhibition and *in situ* catalyst regeneration

Yongbo Kuang[1,2], Qingxin Jia[1,2], Guijun Ma[1,2], Takashi Hisatomi[1,2], Tsutomu Minegishi[1,2], Hiroshi Nishiyama[1,2], Mamiko Nakabayashi[2,3], Naoya Shibata[3], Taro Yamada[1,2], Akihiko Kudo[2,4] and Kazunari Domen[1,2]*

Photoelectrochemical (PEC) water splitting offers a means for distributed solar hydrogen production. However, the lack of stable and cost-effective photoanodes remains a bottleneck that hampers their practical applications. Here we show that particulate Mo-doped $BiVO_4$ water oxidation photoanodes, without costly and complex surface modifications, can possess comparable stability to that of solar cells. The photoanode exhibits enhanced intrinsic photocorrosion inhibition and self-generation and regeneration of oxygen evolution catalysts, which allows stable oxygen evolution for >1,000 h at potentials as low as 0.4 V versus the reversible hydrogen electrode. The significantly improved photocorrosion resistance and charge separation are attributed to the unusual high-temperature treatment. *In situ* catalyst regeneration is found to be a site-specific and oxygen evolution rate change-induced process. Our findings indicate the potential of PEC water splitting to compete with other solar hydrogen production solutions, and should open new opportunities for the development of feasible PEC water splitting systems.

Cost-efficient solar energy conversion has attracted considerable research interest because of the promise of becoming the primary renewable energy source for a sustainable society[1]. Solar hydrogen production by photoelectrochemical (PEC) water splitting offers a promising route to address the intermittency and storage problem of solar energy[2–5]. In addition to production and installation cost, the lifetime of PEC devices plays an essential role in dictating the overall cost[6,7]. Hence, it is important and urgent to demonstrate that photoelectrodes can be sufficiently stable to meet the demand for plant-scale operation. However, the realization of long-term stability has proved to be very demanding, especially for photoanodes, because of photoanodic corrosion and the lack of stable oxygen evolution catalysts (OECs).

Among various materials used for photoanodes, metal oxides are in general considered more stable[8], and $BiVO_4$ is regarded as one of the most promising candidates due to its appropriate bandgap and onset potential[9]. However, there remain two critical challenges. First, $BiVO_4$ is known to be prone to photocorrosion[10]. Surface modifications by OECs are reported to retard the process[11,12], while more effective inhibition of photocorrosion is achieved only by preventing $BiVO_4$ from coming into contact with the electrolyte by means of dense coatings of FeOOH (ref. 13,14) or TiO_2 (ref. 15) to deliver up to a few tens of hours of stability. Second, the activity of co-catalyst layers, which are usually extremely thin to facilitate charge transfer and to avoid charge accumulation, does not always remain constant because of structural changes during operation and loss of catalyst materials due to agitation and dissolution. For example, at an overpotential of 350 mV in 1 M KOH electrolyte, CoOOH, the active phase of Co-based OECs[16], loses about 16% of its activity after 2 h, as the less active cobalt oxide forms during water oxidation[17,18]; and FeOOH suffers from about 44% loss of its mass after 2 h, due to irreversible dissolution[17,19]. Although Ni- and Co-based OECs have been reported to reverse catalyst dissolution in borate and phosphate buffers through a self-repair process[20,21], their practical long-term stability established via this process has yet to be demonstrated. Furthermore, the reported catalyst self-repair usually involves relatively thick layers of OECs, and the layer thickness at equilibrium during operation is hardly controllable, making it difficult to apply to thickness-sensitive applications—for example, as co-catalyst for photoanodes.

Herein, we report the demonstration of ultrastable PEC water splitting using $BiVO_4$ photoanodes at potentials as low as 0.4 V versus reversible hydrogen electrode (RHE). It is found that stability of over 1,000 h can be achieved through simultaneously addressing the photocorrosion of $BiVO_4$ particles, by improving their intrinsic resistivity with a high-temperature treatment, and the degradation of Fe-incorporated Ni-based OECs, by *in situ* on-demand catalyst regeneration. We also show that particle-type $BiVO_4$ electrodes can be made as efficient as state-of-the-art nanostructured electrodes by tuning various properties of the particles, and OEC self-generation can be realized by an integrated design of particulate electrode.

Particulate electrode fabrication and characterization

We fabricated the electrodes from Mo-doped $BiVO_4$ particles that were synthesized by modifying a liquid solid reaction[22], using an improved particle transfer method[23], dedicated for $BiVO_4$. The

---

[1]Department of Chemical System Engineering School of Engineering, The University of Tokyo, 7-3-1 Hongo, Bunkyo-ku, Tokyo 113-8656, Japan. [2]Japan Technological Research Association of Artificial Photosynthetic Chemical Process (ARPChem), 7-3-1 Hongo, Bunkyo-ku, Tokyo 113-8656, Japan. [3]Institute of Engineering Innovation, The University of Tokyo, 2-11-16 Yayoi, Bunkyo-ku, Tokyo 113-8656, Japan. [4]Department of Applied Chemistry Faculty of Science, Science University of Tokyo, 1–3 Kagurazaka, Shinjuku-ku, Tokyo 162-8601, Japan. *e-mail: domen@chemsys.t.u-tokyo.ac.jp

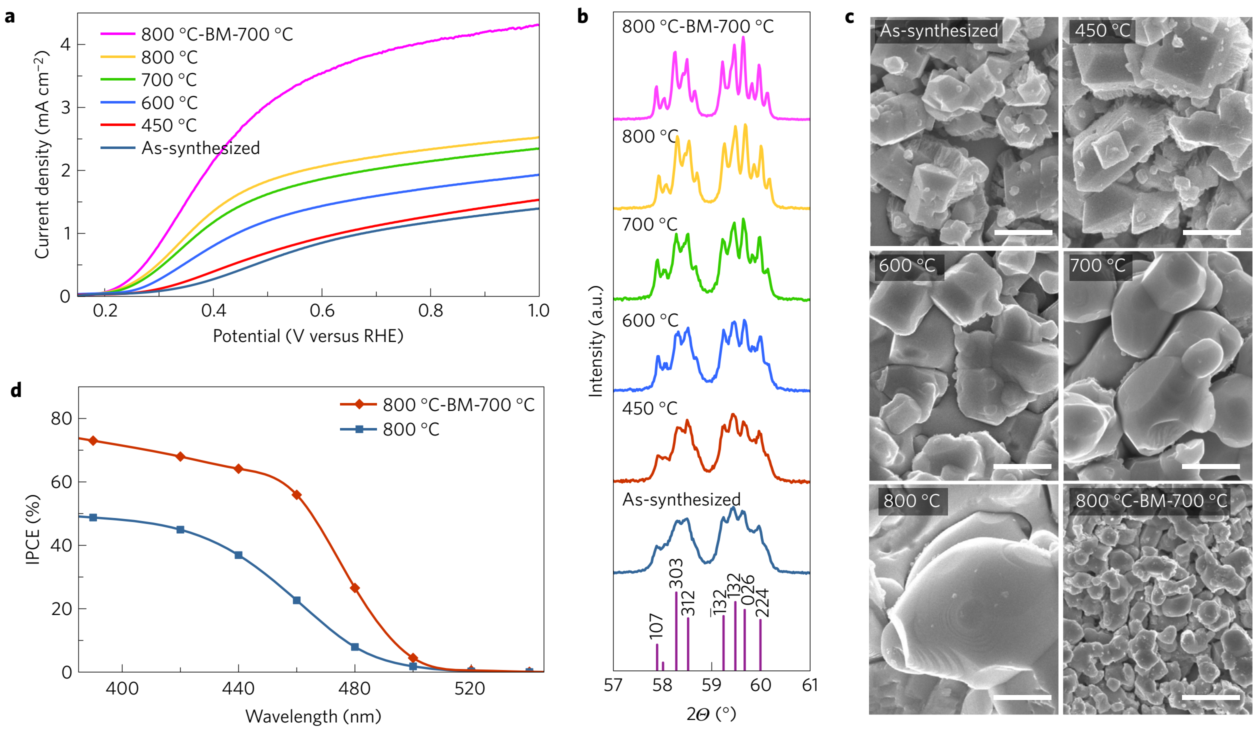

Figure 1 | Characterization of bare 0.3 at.% Mo-doped $BiVO_4$ electrodes. a, Current–potential curves for sulfite oxidation in 0.2 M sodium sulfite containing 1 M potassium borate buffer at pH 9 under AM 1.5G irradiation comparing the charge separation abilities of bare Mo-doped $BiVO_4$/Ni/Sn electrodes prepared using as-synthesized particles, particles annealed at various temperatures (as shown in the legend), and particles treated by 800 °C annealing followed with ball milling and 700 °C post-annealing (800 °C-BM-700 °C). **b**, Narrow-range XRD patterns of the same set of Mo:$BiVO_4$ particles (see Supplementary Fig. 3 for wide-range XRD data). The standard XRD pattern for monoclinic $BiVO_4$ is shown at the bottom (JCPDS, No. 83-1699). **c**, SEM images of the same set of electrodes. Scale bars, 1 μm. **d**, The IPCEs for sulfite oxidation at 0.6 V versus RHE of $BiVO_4$ electrodes prepared from 800 °C annealed particles and 800 °C-BM-700 °C. Fitted lines added as a guide to the eye.

resulting electrode has a monolayer of $BiVO_4$ particles laid over a Ni contact layer (∼500 nm) and a subsequent Sn conducting layer (∼4 μm), and is denoted as Mo:$BiVO_4$/Ni/Sn hereafter. The charge separation properties were examined in the presence of sulfite, used as an efficient hole scavenger. The PEC properties of Mo:$BiVO_4$ particles were optimized by tuning their crystallinity and average particle size through combined annealing and ball-milling treatments, along with doping concentration adjustments. The optimal Mo doping concentration was determined to be 0.3 atomic percent (at.%) (Supplementary Figs 1 and 2).

Figure 1a shows the photocurrents of electrodes prepared with Mo(0.3 at.%):$BiVO_4$ particles treated under various conditions. The photocurrents increased gradually as the annealing temperature was raised from 450 °C to 800 °C, which also improved the crystallinity of the particles, as indicated by sharper peaks in the X-ray diffraction (XRD) patterns (Fig. 1b) and the average particle sizes (Fig. 1c). The positive effect of improved crystallinity seems to prevail over the negative effect of increased particle size for charge separation. Therefore, we expected a better performance for $BiVO_4$ powders that possess both improved crystallinity and reduced particle size to facilitate charge transfer. The samples pre-annealed at 800 °C were ball-milled and again annealed at 700 °C (800 °C-BM-700 °C) to restore the crystallinity. The resulting samples had particle sizes in the range 300–500 nm and showed similarly sharp XRD patterns to the 800 °C annealed samples. The electrode exhibited an improvement in PEC performance. The incident photon-to-current conversion efficiency (IPCE) before and after particle size reduction are compared in Fig. 1d, revealing the effectiveness of size reduction for improving the IPCEs at longer wavelengths.

The intrinsic photocorrosion inhibition property of bare 800 °C-BM-700 °C electrodes was studied by comparing the change of PEC performance, indicated by the photocurrents for sulfite oxidation, before and after being exposed to AM1.5G irradiation for a given time at 1.2 V versus RHE in 0.5 M sodium phosphate buffer at pH 7 in the absence of sulfite. To avoid any effect of Ni species, Ti was used instead for electrode fabrication. A nanoworm $BiVO_4$ electrode with top-level stability among reported systems was measured in parallel as reference[24]. As presented in Fig. 2a, the PEC performance of the high-temperature-treated sample showed an initial increase of about 4% for the first 30 min, probably due to the removal of surface states by this treatment, and then become basically stable for another 1.5 h of exposure. In contrast, the nanoworm electrode suffered from a constant drop in PEC performance for each 30 min of treatment, and lost more than 40% of its initial photocurrent after 2 h. The resulting nanoworm electrode suffered from obvious dissolution of $BiVO_4$, as indicated by the comparison of photos taken before and after the process (Supplementary Fig. 4a). Indeed, the $BiVO_4$ layer of a fresh nanoworm electrode can be almost fully dissolved upon several hours of such treatment.

To confirm that this phenomenon is a photo-induced electrochemical process, the nanoworm electrodes were biased at 0.6 V versus RHE under AM1.5G irradiation or at 1.2 V in dark (Fig. 2b). Interestingly, in both cases, no obvious drop in PEC performance was observed within 2 h of treatment, which is in sharp contrast to the rapid decrease shown in Fig. 2a. In fact, without irradiation, the $BiVO_4$ electrodes do not suffer from dissolution or performance drop even at potentials as high as 2 V versus RHE, as confirmed with both types of electrode (Supplementary Fig. 5a). However, when exposed to light, the nanoworm electrode did suffer from much faster photocorrosion, and the $BiVO_4$ layer was almost fully dissolved within 2 h (Supplementary Fig. 5b). These results

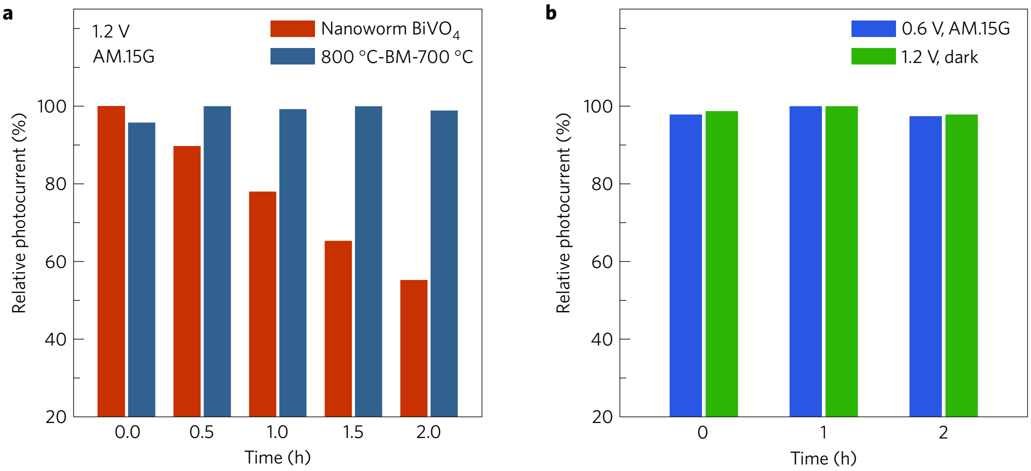

Figure 2 | Photocorrosion inhibition properties of bare 800 °C-BM-700 °C/Ti/Sn electrodes. The photocorrosion inhibition properties of the electrodes were examined by comparing the photocurrent for sulfite oxidation in borate buffer (pH 9) containing 0.2 M sodium sulfite before and after performing photooxidation of water in 0.5 M sodium phosphate buffer (pH 7) in the absence of sulfite at various conditions. The previously reported nanoworm $BiVO_4$ electrodes were also examined using front illumination for comparison[24]. **a**, Changes in photocurrent for sulfite oxidation after a bare 800 °C-BM-700 °C/Ti/Sn electrode or a bare nanoworm electrode photooxidized water at 1.2 V versus RHE in 0.5 M sodium phosphate buffer (pH 7) for 2 h with a 30 min interval. **b**, Changes in photocurrent for sulfite oxidation after a nanoworm electrode photooxidized water in 0.5 M sodium phosphate buffer (pH 7) at 0.6 V versus RHE under illumination or at 1.2 V versus RHE in dark for 2 h with a 1 h interval. AM 1.5G illumination was used for all photocurrent measurements. See Supplementary Fig. 4 for the current–time plots obtained during photooxidation of water.

clearly indicate that neither the irradiation nor the high applied bias alone causes the observed dissolution, and that the dissolution process relies on the surface-reaching photogenerated holes. By comparing the recorded photocurrents under different conditions in phosphate solution (Supplementary Figs 4 and 5), it is revealed that the rate of dissolution of the nanoworm $BiVO_4$ electrode is proportional to the observed photocurrents. Therefore, this photocorrosion process is indeed photo-induced electrochemical dissolution of $BiVO_4$. Because the electrolyte solution contained dissolved oxygen, as the experiments were carried out in air, oxygen is thus unlikely to play a role in the dissolution process. So there must be other intermediate species generated during water oxidation by the holes under irradiation—for example, hydroxyl radical and hydrogen peroxide. Further studies would be required to identify such intermediate species and to understand the detailed mechanism for the dissolution.

Since the same magnitude of photocurrents was also observed with the 800 °C-BM-700 °C electrode in phosphate solution (Supplementary Fig. 4b), both types of electrode should suffer from a similar corrosive local environment. However, the decay in PEC performance was not observed for the 800 °C-BM-700 °C electrode, which clearly suggests significantly enhanced resistance to the photo-induced electrochemical dissolution. As it is not observed with other particulate[25], or Mo-doped $BiVO_4$ electrodes[26,27], the enhanced intrinsic photocorrosion inhibition is hence correlated with the improved crystallinity due to the thermal treatment.

Although the high crystallinity obtained with unusual high-temperature (800 °C) annealing is clearly demonstrated here to benefit both the charge transport and photocorrosion resistance for Mo:$BiVO_4$ electrodes, previously studied systems are generally annealed below 500 °C. This is reasonable because, when treated above that temperature in air, the FTO and ITO substrates used for film-type $BiVO_4$ electrodes become much less conductive; and intrinsic $BiVO_4$ suffers from decreased carrier density due to loss of oxygen vacancies, albeit the increase of crystallinity with annealing temperature is shown to be independent of doping concentration (Supplementary Fig. 6). With sufficient Mo doping, the $BiVO_4$ particles can survive high-temperature annealing without their carrier density being much affected (Supplementary Fig. 1).

In situ self-generation of oxygen evolution catalyst

We activated Mo:$BiVO_4$/Ni/Sn in a freshly prepared borate buffer electrolyte without any prior surface modification. The Mo:$BiVO_4$/Ni/Sn electrode was biased at an anodic potential of 0.6 V versus RHE under simulated AM 1.5G solar irradiation. The photocurrent initially increased rapidly, reaching a maximum plateau after about 2 h. Figure 3a shows the change of photocurrent; the insets show the scanning electron microscopy (SEM) image and the photocurrent–potential curve obtained for the fully activated OEC-decorated electrode, which exhibits a rapid increase in photocurrent at potentials below 0.6 V versus RHE. After the pretreatment, the surfaces of $BiVO_4$ particles were well covered with an amorphous layer about 5 nm in thickness, as observed in the high-resolution transmission electron microscopy (HRTEM) image (Fig. 3b), which are the OECs. The current–potential behaviour in a two-electrode configuration was measured with a Pt plate counter electrode, and the maximum applied bias photon-to-current efficiency (ABPE) is calculated to be about 1.6% under such conditions (Fig. 3c).

The Ni underlayer is considered to work as the ion source for the deposition of the OECs. When we started the activation process by applying an oxidative potential, the exposed metallic surfaces of the Ni contact layer of the Mo:$BiVO_4$/Ni/Sn electrode will be immediately oxidized to form a thin passivation layer that prevents further oxidation of Ni, as evidenced by the negligible dark currents. As $Ni(OH)_2$ is slightly soluble in pH 9 borate buffer[28], the passivation layer, composed of NiO and $Ni(OH)_2$, thus serves as the source for dissolved Ni^{2+} ions. Because the passivation layer is so close to the $BiVO_4$ particles, the dissolved Ni^{2+} can have a much higher local concentration to facilitate the OEC deposition, although its concentration in the bulk solution is much lower. Upon irradiation, Ni^{2+} will be oxidized by the holes from $BiVO_4$ and deposit as Ni-(oxy)hydroxide/borate on the surface of the $BiVO_4$ particles in the borate buffer[28]. It should be noted that because the dissolution of Ni^{2+} species from the passivation layer is rather limited, the Ni^{2+} concentration after long-term stability tests is still below the critical level that would cause excessive OEC deposition under our test conditions, as will be discussed later.

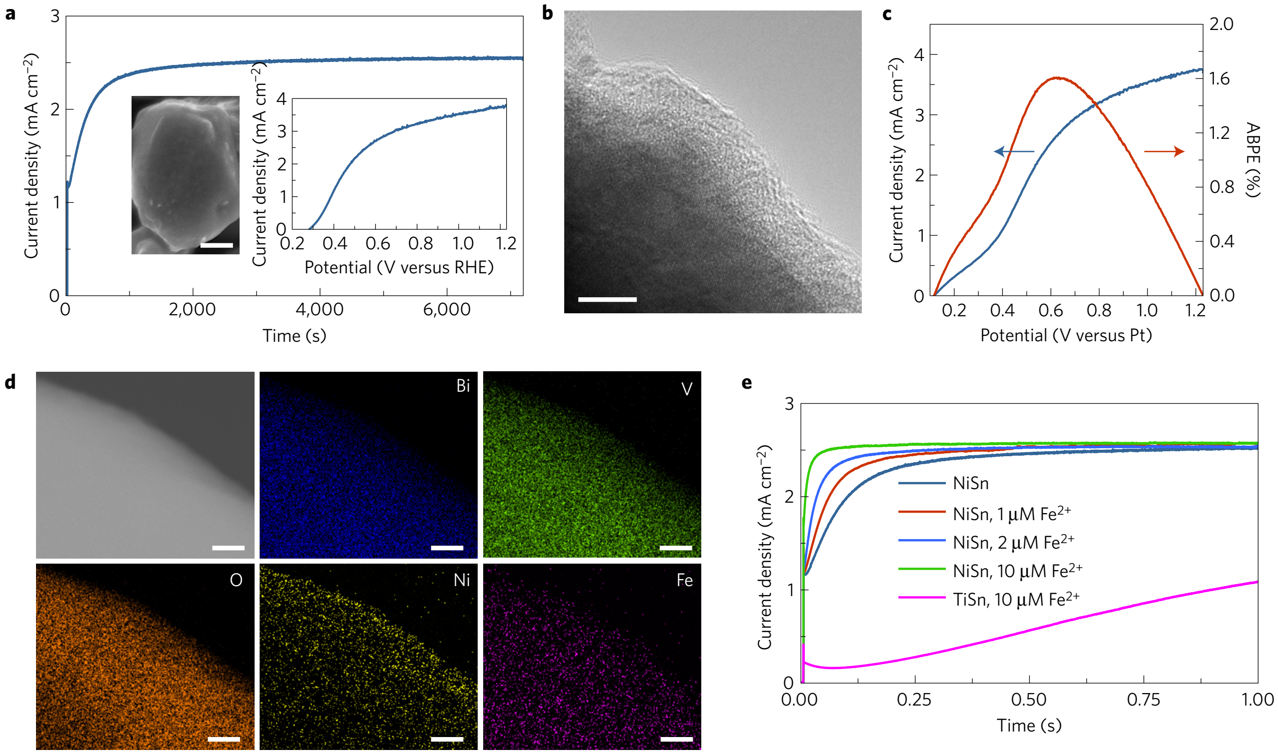

Figure 3 | Catalytic activation of Mo:$BiVO_4$/Ni/Sn electrodes and characterization. **a**, Photocurrent change of a bare Mo:$BiVO_4$/Ni/Sn in a fresh 1 M borate buffer under AM 1.5G irradiation at 0.6 V versus RHE. The rapid increase in photocurrent indicates the self-generation of OECs. The insets are the SEM image of the electrode taken after catalyst modification (scale bar, 100 nm), and the current–potential curve of the activated electrode. **b**, HRTEM image of the $BiVO_4$ particles after catalytic activation. Scale bar, 5 nm. **c**, Photocurrent–potential curve and ABPE of the activated electrode measured using a two-electrode configuration with a Pt plate counter electrode. **d**, STEM–EDS elemental mapping images of the $BiVO_4$ particles after catalytic activation. Scale bars, 20 nm. **e**, Changes of photocurrents of Mo:$BiVO_4$/Ni/Sn electrodes in the presence of various concentrations of added Fe^{2+} in 1 M borate buffers under AM1.5G irradiation. Mo:$BiVO_4$/Ti/Sn electrode was also measured in a borate buffer containing 10 μM Fe to show the critical role of a Ni contacting layer for OEC generation. The values of Fe^{2+} concentration represent the amounts of Fe intentionally added.

Without Fe species, Ni-based OECs are much less active catalysts for water oxidation, as have been reported recently[29,30]. Even a trace amount of Fe impurities in the electrolyte solutions has been found to be critical for the activities of Ni-based OECs, and the presence of Fe species has been demonstrated to be unavoidable for near-neutral and alkaline electrolytes[28,31]. Thus, we anticipated that Fe impurities in the borate buffer should also play a similarly important role for the high activity of our self-generated OECs. As expected, the presence of Fe species on the surface of the $BiVO_4$ particles after catalytic activation was confirmed by scanning transmission electron microscopy–energy dispersive X-ray spectroscopy (STEM–EDS) elemental mapping (Fig. 3d). The Fe:Ni ratio in the catalyst layer was also found to increase from 11:89 after 1 h of catalytic activation to 28:72 after 2 h of catalytic activation by X-ray photoelectron spectroscopy (XPS) analysis (Supplementary Fig. 7a).

We then examined the effect of Fe^{2+} additives for the activation of self-generated OECs over Mo:$BiVO_4$/Ni/Sn (Fig. 3e). As the concentration of Fe^{2+} was raised, the activation proceeded more rapidly to reach the same level of photocurrent. Clearly, the activation process depends on Fe^{2+} to reach the plateau photocurrent value, consistent with recent literature reports[28–30]. The resulting samples showed a similar Fe percentage (of about 30%) in the total metal content of the catalyst layer. The effect of direct FeOOH deposition on this phenomenon can be excluded again by using a Ni-free Mo:$BiVO_4$/Ti/Sn electrode immersed in a borate solution containing 10 μM of Fe^{2+}. The result suggests that the direct FeOOH deposition is too slow to have any effect. Therefore, it is inferred that Fe impurity incorporation occurs immediately following the start of Ni deposition to form the more active NiFe-mixed material, and the rate of Fe incorporation depends heavily on the concentration of dissolved Fe^{2+} ions. Hereafter we designate the present self-generated co-catalyst as 'NiFe-OEC'.

The stoichiometric evolution of oxygen and hydrogen for the fully activated electrode was confirmed by gas chromatography in a gas-tight flow system. A time course of excellent faradaic efficiency, calculated using recorded photocurrents and detected gas evolution, was obtained for both oxygen and hydrogen evolution (Supplementary Fig. 8).

Water splitting stability and *in situ* catalyst regeneration

The long-term stability of the activated Mo:$BiVO_4$/Ni/Sn electrode was investigated with the potential controlled at 0.6 V versus RHE in fresh 1 M borate buffers at pH 9. At 25 °C, with temperature control, the electrode exhibited an incredible stability in a continuous 400-h test, without an obvious photocurrent drop (Fig. 4a). The SEM image of the electrode taken after the stability test indicates no detectable change in morphology and OEC coverage.

A continuous test for one single Mo:$BiVO_4$/Ni/Sn electrode was performed at 0.6 V versus RHE for a total of 1,100 h without temperature control, as shown in Fig. 4b. This test was separated into eleven 100-h runs; between any two runs, the electrode was removed from the electrolyte, rinsed with pure water, and then dried. In these off-periods the electrolyte was replaced with fresh pure borate buffer of the same content. Although fresh Ni^{2+}-free solution was supplied at the beginning of each run, the photocurrent did not decrease, indicating that the catalytic activity of NiFe-OECs remained operative during the intervals.

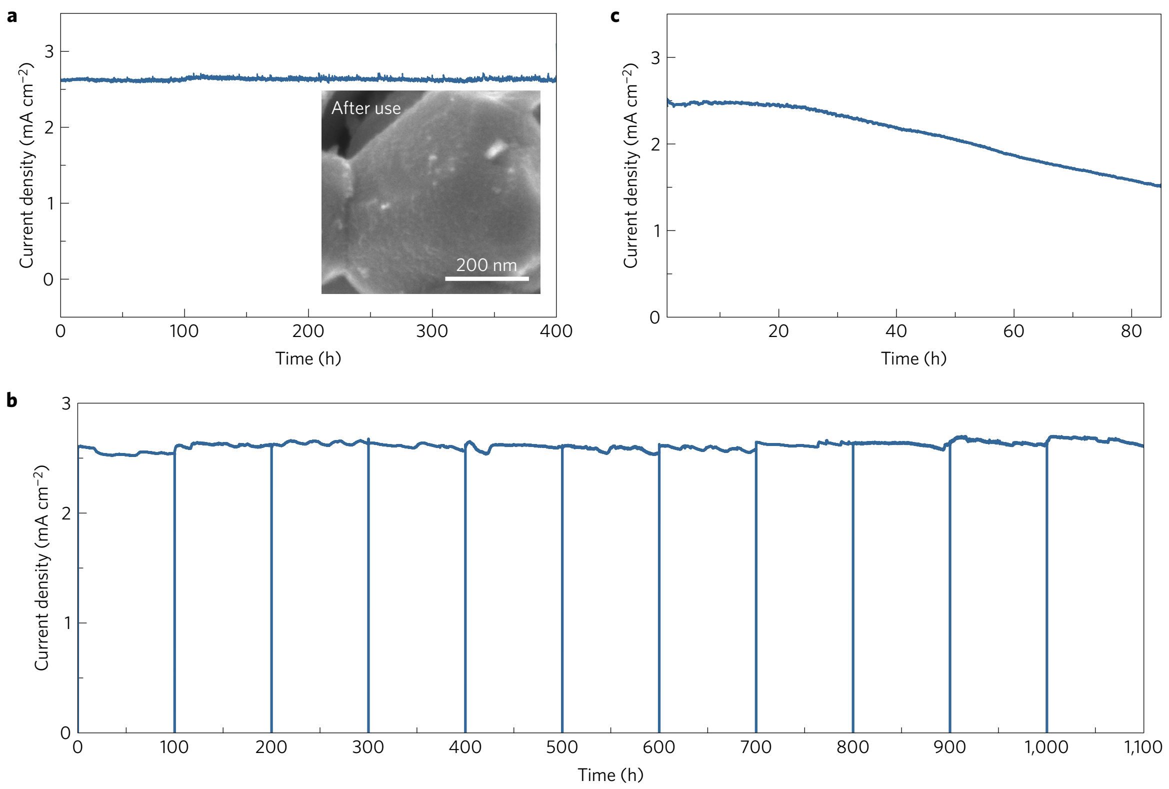

Figure 4 | Long-term water oxidation stability of activated Mo:BiVO$_4$/Ni/Sn electrodes. a, 400-h water splitting with a NiFe-OEC/Mo:BiVO$_4$/Ni/Sn electrode at 0.6 V versus RHE in a fresh 1 M borate buffer at 25 °C under AM1.5G irradiation. The inset shows the SEM image of the electrode after 400-h water splitting. **b**, 1,100-h discontinuous water splitting with a NiFe-OEC/Mo:BiVO$_4$/Ni/Sn electrode at 0.6 V versus RHE under AM1.5G irradiation measured without temperature control. The same BiVO$_4$ particle electrode was repetitively used for 100-h water splitting in fresh borate buffers for 11 runs with an overall duration of 1,100 h. **c**, Stability of a NiFe-OEC/Mo:BiVO$_4$/Ti/Sn electrode in a fresh 1 M borate buffer at 0.6 V versus RHE under AM1.5G irradiation.

The measured photocurrent fluctuated within 15%, mainly due to the daily and occasional changes of ambient temperature between 18 and 25 °C.

In addition, we examined the effect of applied voltage on the water oxidation stability of our BiVO$_4$ electrodes (Supplementary Fig. 10 and 11). The electrode was stable for a wide range of potentials greater than 0.4 V versus RHE, which is an important feature if it is to be coupled with photocathodes with different working potentials to assemble stand-alone overall PEC water splitting devices with a parallel configuration. However, tandem configuration is not applicable in this case due to the non-transparency of the BiVO$_4$ electrode. The working potentials in the low-bias range of 0.4–0.8 V versus RHE are practical values for such applications. Photoanodes that require far more positive anodic working potentials are unsuitable for this purpose[32–34]. Moreover, although BiVO$_4$ is chemically more stable than most materials used for solar cells (for example, silicon) in aqueous media, stabilizing BiVO$_4$-based electrodes at potentials below 1.23 V versus RHE has been shown to be more challenging than stabilizing silicon photoanodes at much higher potentials with a similar protection approach[15,33], highlighting the effectiveness of our approach. The present stability results represent a significant step in enhancing durability for water splitting photoanodes, demonstrating the great potential of PEC water splitting technique to meet the requirements of industry regarding lifetime.

The high stability of the Mo:BiVO$_4$/Ni/Sn is found to be due to the presence of dissolved Ni^{2+} ions, as suggested by the results using a NiFe-OEC-decorated Mo:BiVO$_4$/Ti/Sn electrode, shown in Fig. 4c. The NiFe-OEC was anodically deposited from a borate buffer containing 5 μM of Ni^{2+} and 10 μM of Fe^{2+} and was well activated. Then the electrode was used for stability tests in a fresh borate buffer free of Ni^{2+} species. The electrode was relatively stable for the first 10 h, but became gradually less active with prolonged operation due to OEC dissolution or exfoliation. The lower stability of this electrode, as compared to the Mo:BiVO$_4$/Ni/Sn electrode, implies the existence of an *in situ* catalyst regeneration process and the important role of Ni^{2+} species in it, when Ni is used as the contact layer.

On the basis of above results, the overall mechanism for NiFe-OEC self-generation and *in situ* regeneration of Mo:BiVO$_4$/Ni/Sn electrodes is proposed as shown in Fig. 5. The proposed mechanism consists of four key steps, which are the passivation of the Ni layer and the dissolution of Ni^{2+} ions, the photoelectrodeposition of Ni-OEC, the incorporation of Fe^{2+} to generate NiFe-OEC, and self-regeneration of NiFe-OEC during long-term operation.

To further understand the mechanism behind this catalyst regeneration process, we investigated the effect of Ni^{2+} concentration on electrode activation and long-term performance. After a 400-h stability measurement of activated Mo:BiVO$_4$/Ni/Sn in initially Ni^{2+}-free electrolyte, the final Ni^{2+} concentration in the electrolyte was measured by inductively coupled plasma-atomic emission spectroscopy (ICP-AES) to be less than 1 μM. The total Ni consumption is thus calculated to be no more than 1%, which is demonstrated to have no impact on the electrical conductivity and mechanical strength of the electrode. With exactly 1 μM of pre-added Ni^{2+}, no obvious reduction in the photocurrents was observed with activated Mo:BiVO$_4$/Ni/Sn (Fig. 6a).

On a bare Mo:BiVO$_4$/Ti/Sn electrode, when 0.5 μM of Ni^{2+} was added during a photocurrent–time measurement, it led to a

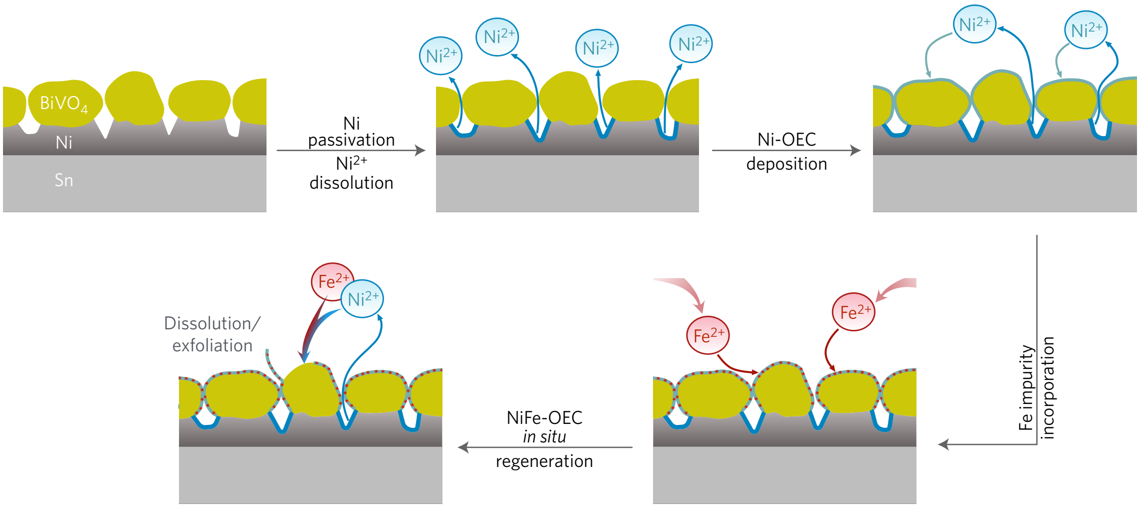

Figure 5 | Schematic illustration of NiFe-OEC self-generation and *in situ* regeneration. Upon electrochemical oxidation, the Ni contacting layer of the Mo:$BiVO_4$ electrode is oxidized to form a thin passivation layer, which serves as the source of dissolved Ni^{2+} ions. Under irradiation, Ni-based catalyst (Ni-OEC) is photoelectrochemically deposited over the surface of Mo:$BiVO_4$ via the photooxidation of Ni^{2+} ions. Ni-OEC is then transformed into a more active catalyst (NiFe-OEC) through the incorporation of Fe species, which are impurities that originate from the freshly prepared borate electrolytes. During long-term water splitting, *in situ* regeneration of NiFe-OEC using the dissolved Ni and Fe species takes place where the loss of catalyst occurs due to dissolution or exfoliation, such that the PEC performance can be maintained.

sudden rise in photocurrent (Fig. 6b). The activation process of Mo:$BiVO_4$/Ti/Sn electrodes was also examined with initial additions of 0.5 and 1 μM of Ni^{2+}. It is clear that the higher Ni^{2+} concentration results in faster catalyst deposition to reach the same plateau photocurrent (Fig. 6c). However, when 2 μM of Ni^{2+} was initially added, the photocurrent started to decrease after reaching the photocurrent maximum, without exhibiting the photocurrent plateau stage.

This photocurrent decline at 2 μM of Ni^{2+} is due to catalyst 'overloading', because increasing loading of Ni-based catalyst not only improves the catalytic activity[35], but also increases the chance for surface charge recombination for photoanodes due to charge accumulation near the interface caused by the oxidation of Ni^{2+} to Ni^{3+}/Ni^{4+} (ref. 30); when catalyst overloading occurs, the effect of charge recombination prevails, resulting in reduced photocurrents[36]. Fortunately, our Mo:$BiVO_4$/Ni/Sn electrodes never released Ni^{2+} concentrations higher than 1 μM into the operational solution; thus, the high activity of the electrodes persisted.

These results imply that NiFe-OEC loading does not further increase after full activation at Ni^{2+} concentrations below 1 μM, and the saturation amount of catalyst loading is independent of Ni^{2+} concentration, otherwise a photocurrent plateau stage would appear before the decline in Fig. 6c. This phenomenon is analogous to Langmuir monolayer adsorption after saturation[37], where the adsorption becomes independent of adsorbate pressure. A possible explanation could be made by considering the activity and selectivity for Ni^{2+} and water oxidation at the surface of the photoanode. Before complete activation, the surface is active for both reactions. With increasing catalyst loading, the surface becomes more active for water oxidation because NiFe-OEC is among the most active OECs known so far[30]. When the catalyst layer reaches its optimum thickness of about 5 nm, as observed in the HRTEM image (Fig. 3d), the surface becomes selectively active for water oxidation, and the oxidation of Ni^{2+} ceases to proceed. During long-term operation, the loss of water oxidation activity occurs due to catalyst dissolution or exfoliation, leaving inactive sites on the Mo:$BiVO_4$ surface. Although less active, those sites are more selective for Ni^{2+} oxidation to allow for the re-deposition of catalyst to restore the activity and selectivity, and to maintain the coverage and thickness of the catalyst layer, as confirmed by the HRTEM image of the sample after a 100 h stability test (Supplementary Fig. 9). This mechanism thus explains the important site-specific feature of the *in situ* catalyst regeneration process (Fig. 6d).

At higher Ni^{2+} concentrations, the oxidation of Ni^{2+} at the sites saturated with NiFe-OEC can no longer be ignored. The catalyst deposition then becomes non-site-specific (Fig. 6d), and will cause catalyst overloading all over the Mo:$BiVO_4$ surface. In the present case this high Ni^{2+} concentration was never reached just by the existence of a passivated Ni contact layer in Mo:$BiVO_4$/Ni/Sn as the source for Ni^{2+}.

Effect of electrolytes

$BiVO_4$ electrodes have been mostly investigated in neutral and near-neutral electrolytes[9,11,38], which is indeed a great advantage because these media are less corrosive and more environmentally benign; in contrast, electrodes based on nitrides and oxynitrides favour strong alkaline conditions for better performance and stability[39–41]. There is also work reported on stabilizing $BiVO_4$ electrodes for use in alkaline electrolytes[15,42,43], as the electrodes are regarded to benefit from better electrolyte conductivity and a lower pH gradient. Buffering reagents, such as phosphate[44], carbonate and borate[45,46], are usually used for neutral and near-neutral electrolytes to achieve similar effects. In this case, the high concentration of borate buffer is important in reducing the electrical resistance of the solution and in facilitating mass transfer (Supplementary Fig. 12). On ceasing agitation, a new equilibrium is established within 30 s and the photocurrent becomes stable again after an initial drop of less than 3%. Such a feature can be important in practice to reduce the external power consumption.

Phosphate buffer electrolytes have been previously shown to slowly dissolve $BiVO_4$ (ref. 24). Although not suitable for long-term applications, it would be interesting to investigate if phosphate-containing electrolytes act as appropriate media for the NiFe-OEC regeneration process. However, it turned out that they are not compatible with Ni-based catalysts because phosphate ions greatly accelerate dissolution of the catalysts (Supplementary Figs 13–15).

Conclusions

We have realized practical long-term stability (>1,000 h) at low working potentials for PEC water splitting using robust, particulate Mo:$BiVO_4$ photoanodes in which OECs are generated

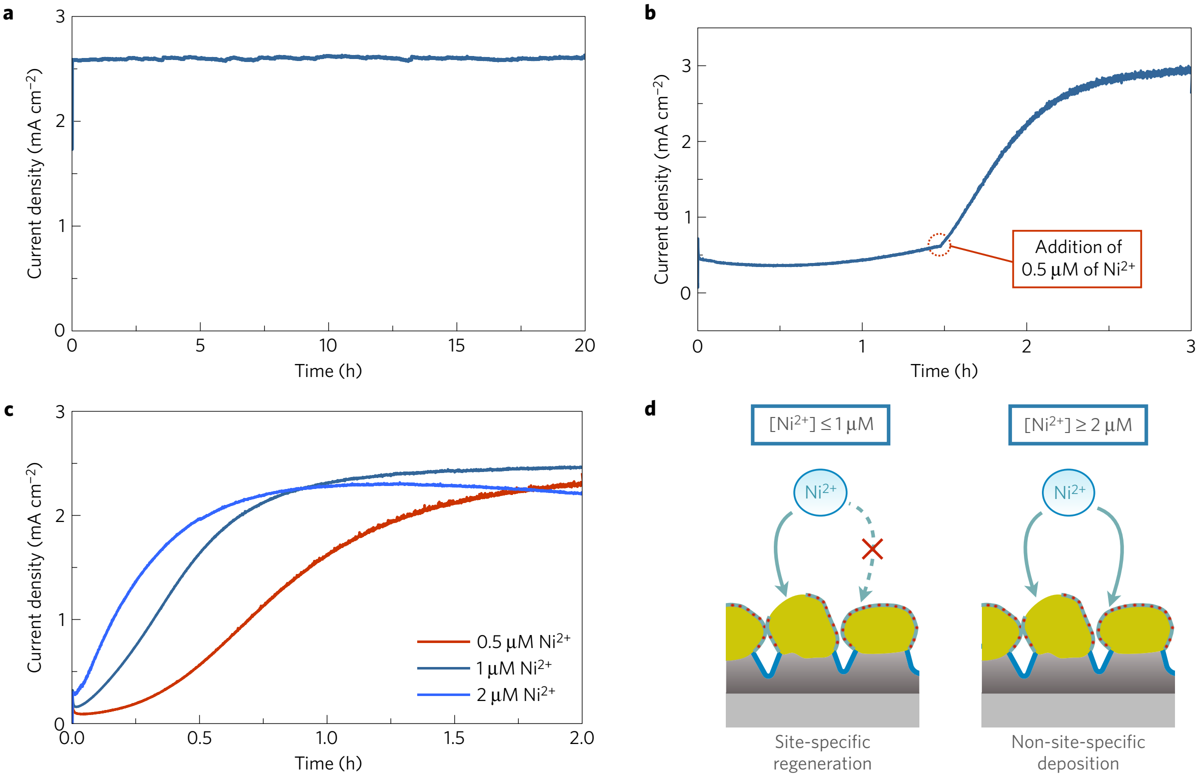

Figure 6 | Effect of Ni^{2+} concentration on catalyst formation and regeneration. a, 20 h stability of an activated $Mo:BiVO_4/Ni/Sn$ electrode for water oxidation at 0.6 V in a 1 M borate buffer containing 1 µM of Ni^{2+}. **b**, Change of photocurrents of a $Mo:BiVO_4/Ti/Sn$ electrode upon a sudden addition of 0.5 µM Ni^{2+} at 1 V versus RHE in a fresh 1 M borate buffer. **c**, Photocurrent–time curves of bare $Mo:BiVO_4/Tn/Sn$ electrodes at 0.6 V versus RHE in 1 M borate buffers containing 0.5 µM, 1 µM and 2 µM of Ni^{2+} ions, respectively. The photocurrent started to decrease after about 1 h for 2 µM of Ni^{2+}, although it increased initially. **d**, Schematic comparison of the site-specific catalyst regeneration and non-site-specific catalyst deposition process in a 1 M borate buffer at pH 9. When the concentration of Ni^{2+} is below 1 µM, the re-deposition of Ni-based catalyst occurs selectively at sites that suffer from the loss of catalyst because these sites are more active for Ni^{2+} oxidation, while the sites saturated with NiFe-OEC are more active for water oxidation. At higher concentrations of Ni^{2+}, Ni^{2+} oxidation becomes non-site-specific as its reactivity increases, leading to catalyst overloading.

and regenerated *in situ*. The advantage of particulate $BiVO_4$ electrodes is the ease with which the properties of powders can be tuned before fabrication into electrodes. The high-temperature treatment enabled by Mo doping substantially improves the intrinsic stability of $BiVO_4$ against photocorrosion, which is difficult to apply for the thin-film $BiVO_4$ electrodes. We also demonstrate the concept of integrated photoanodes, which incorporate a thin layer of Ni that simultaneously acts as an electrical back contact and as an ion source to allow *in situ* self-generation of catalyst. A catalyst regeneration process, which ensures selective NiFe-OEC re-deposition where catalytic activity decreases due to loss of catalyst, is found to be essential for the sustained catalytic activity.

Our present strategy will be applied in the future development of particulate photoelectrodes based on other photo-absorbers that are active over a wider solar spectrum. Furthermore, our results also pave the way towards developing highly efficient printable electrodes by inkjet printing, with the promise of further reductions in production costs. Most importantly, we believe that the OEC *in situ* regeneration mechanism demonstrated here will be of great use in enhancing the economic and industrial viability of PEC water splitting devices.

Methods

Synthesis and post-treatment of Mo-doped $BiVO_4$ particles. 0–1 atomic per cent (at.%) Mo-doped $K_3V_5O_{14}$ powders with layered structures as starting materials were obtained by grinding the solids obtained by calcination of K_2CO_3, MoO_3 and V_2O_5 in stoichiometric ratios in air at 450 °C for 5 h. Mo-doped $BiVO_4$ particles were synthesized simply by stirring 4 mmol of Mo-doped $K_3V_5O_{14}$ and 20 mmol of $Bi(NO_3)_3 \cdot 5H_2O$ in 100 ml of water at 70 °C for 10 h. $Bi(NO_3)_3 \cdot 5H_2O$ powder reacts with water to form slightly soluble $BiONO_3$ as a dispersion in water. The as-synthesized Mo-doped $BiVO_4$ particles were annealed at 800 °C for 2 h and crushed twice by ball milling at 800 r.p.m. for 30 min, followed with re-annealing at 700 °C for 2 h.

$BiVO_4$ electrode preparation. Typically, the $BiVO_4$ particles were dispersed in isopropanol (30 mg/2 ml) and sonicated for 1 h to form a homogeneous suspension. 1 ml of dispersed solution was dropcast onto a thin glass substrate (3 × 3 cm) and left to dry slowly under a controlled vapour pressure. The process was then repeated. After drying the solvent, ~0.5 µm of Ni (or Ti) and ~4 µm of Sn were sequentially deposited above the $BiVO_4$ layer by thermal vapour deposition (without exposing to air) to hold the particles mechanically firmly and make an highly electrically conductive contact. There are several advantages to using Sn as the conducting layer. First, it forms stable passivation layer in neutral and near-neutral borate and phosphate buffers, therefore ensuring a satisfactorily low dark current in the range of potentials used for the PEC measurements; second, its low melting point allows easy evaporation of a thick substrate layer to give good mechanical strength and electrical conductivity; third, its low price helps in reducing the overall production cost. The $Sn/Ni/BiVO_4$ film was then peeled off and fixed onto a glass plate by means of adhesive double-sided tape, or epoxy resin for better durability, with excess $BiVO_4$ particles being removed by sonication in water. A copper wire was connected to the electrode using indium solder, with the weld being covered by epoxy resin. The unused surface of the electrode was also masked with epoxy resin.

Characterization. The scanning electron microscopy (SEM) images of $BiVO_4$ electrodes were taken with a Hitachi SU8020 FE-SEM at an accelerating voltage of 5–10 kV. High-resolution transmission electron microscopy (HRTEM) and energy dispersive X-ray spectroscopy (EDS) were carried out with a JEOL JEM-2800 microscope equipped with a X-Max 100LTE SDD detector. X-ray photoelectron spectroscopy (XPS) spectra were collected using a Mg Kα non-chromatic source (14.6 kV, 15 mA, 50 eV pass energy). XPS quantitative analysis was made with a relative sensitivity factor method. The crystal structure and crystallinity of $BiVO_4$ particles prepared under various conditions were examined by powder X-ray diffraction with a Rigaku Smartlab X-Ray Diffractometer operated with a Cu Kα radiation source at 40 kV and 30 mA. The content of Mo in the Mo-doped $BiVO_4$ particles and the concentration of Ni^{2+} in the electrolyte solution were confirmed by inductively coupled plasma-atomic emission spectroscopy (ICP-AES) with a Shimazu ICPS-8100 sequential type ICP emission spectrometer.

Photoelectrochemical measurements. The photoelectrochemical performances of $BiVO_4$ electrodes were measured with a three-electrode configuration using a HSV-100 potentiostat or HZ-7000 potentiostat (Hokuto Denko), a saturated Ag/AgCl ($E_{\mathrm{Ag/AgCl}} = 0.197$ V versus NHE at 25 °C) reference electrode and a Pt wire counter electrode. Typically, electrodes with exposed areas of $\sim$0.2 cm^2 were measured in a glass cell containing 100 ml of electrolyte. The recorded potentials versus Ag/AgCl ($E_{\mathrm{versus\ Ag/AgCl}}$) were converted against reversible hydrogen electrode (RHE) using the Nernst equation below.

$$E_{\mathrm{versus\ RHE}} = E_{\mathrm{versus\ Ag/AgCl}} + E_{\mathrm{Ag/AgCl}} + 0.059\mathrm{pH}$$

A commercial XES-301S solar simulator (SAN-Ei Electric) was used as the light source, and was calibrated to best match the AM1.5G spectra at 100 mW cm^{-2} (ASTM G173-03) using an LS-100 spectroradiometer (EKO Instrument). 1 M potassium borate buffer, prepared by adjusting the pH of 1 M H_3BO_3 solution to 9 with KOH at 25 °C, was used as the electrolyte. For sulfite oxidation, an additional 0.2 M Na_2SO_3 was added to the borate buffer. For the photocorrosion inhibition property study, 0.5 M sodium phosphate buffer at pH 7 was used as the electrolyte. Current–potential curves were recorded in the anodic direction. The scan rate for linear sweep and cycle voltammetry was 20 mV s^{-1}. The applied bias photon-to-current efficiency (ABPE) was calculated from the two-electrode current–potential curves measured under AM1.5G 1 sun illumination and argon bubbling, with a Pt plate counter electrode placed right behind the $BiVO_4$ electrode, using the equation:

$$\mathrm{ABPE} = [(1.23 - V_{\mathrm{Pt}}) \times J_{\mathrm{light}}/P_{\mathrm{light}}] \times 100\%,$$

where V_{Pt} is the applied potential versus Pt counter electrode, J_{light} is the measured photocurrent, and P_{light} (100 mW cm^{-2}) is the power density of AM1.5G. Incident photon-to-current efficiency (IPCE) was measured using a MAX-302 xenon light source (Asahi Spectra) equipped with bandpass filters to provide monochromatic irradiation. The light intensity (P_λ) at each wavelength (λ) was measured using a NOVA II laser power meter equipped with a photodiode PD-300 sensor (Ophir Optronics). IPCE was calculated using the equation below.

$$\mathrm{IPCE} = [(1{,}240/\lambda) \times (J_{\mathrm{light}} - J_{\mathrm{dark}})/P_\lambda] \times 100\%.$$

Photocorrosion inhibition property measurements. The photocorrosion inhibition properties of bare $BiVO_4$ electrodes were examined by comparing photocurrents for sulfite oxidation before and after performing water oxidation in 0.5 M sodium phosphate buffers (pH 7) in the absence of sulfite at various conditions. The sulfite oxidation photocurrents were measured in a 1 M pH 9 borate buffer containing 0.2 M Na_2SO_3 at 0.6 V under AM1.5G irradiation for 1 min. The photocurrent values read at the end of the measurements were used for comparison. The electrodes were scanned (scan rate 40 mV s^{-1}) between 0.15–1.25 V versus RHE for five cycles under illumination before each measurement.

Long-term stability measurements. Long-term stability tests of $BiVO_4$ electrodes for photoelectrochemical water splitting were carried out at 0.6 V versus RHE under simulated AM1.5G irradiation using a three-electrode configuration in fresh 1 M potassium borate solutions at pH 9. The continuous 400-h test was conducted at 25 °C in a water bath with temperature control, and the data was recorded using a VersaSTAT 3 potentiostat (Princeton Applied Research). The discontinuous 1,100-h experiment was implemented without temperature control as eleven separate 100-h runs using a HZ-7000 potentiostat (Hokuto Denko). Between each two runs, the electrode was removed from the electrolyte, rinsed with pure water, dried in air, and the electrolyte was replaced with a fresh one.

Data availability. The data that support the plots within this paper and other findings of this study are available from the corresponding author upon reasonable request.

Received 18 May 2016; accepted 17 November 2016; published 19 December 2016

References

1. Lewis, N. S. & Nocera, D. G. Powering the planet: chemical challenges in solar energy utilization. *Proc. Natl Acad. Sci. USA* **103**, 15729–15735 (2006).
2. Grätzel, M. Photoelectrochemical cells. *Nature* **414**, 338–344 (2001).
3. Lewis, N. S. Toward cost-effective solar energy use. *Science* **315**, 798–801 (2007).
4. Chen, X., Shen, S., Guo, L. & Mao, S. S. Semiconductor-based photocatalytic hydrogen generation. *Chem. Rev.* **110**, 6503–6570 (2010).
5. Walter, M. G. *et al.* Solar water splitting cells. *Chem. Rev.* **110**, 6446–6473 (2010).
6. Hamann, T. Perovskites take lead in solar hydrogen race. *Science* **345**, 1566–1567 (2014).
7. McKone, J. R., Lewis, N. S. & Gray, H. B. Will solar-driven water-splitting devices see the light of day? *Chem. Mater.* **26**, 407–414 (2014).
8. Sivula, K. & de Krol, R. V. Semiconducting materials for photoelectrochemical energy conversion. *Nat. Rev. Mater.* **1**, 15010 (2016).
9. Park, Y., McDonald, K. J. & Choi, K.-S. Progress in bismuth vanadate photoanodes for use in solar water oxidation. *Chem. Soc. Rev.* **42**, 2321–2337 (2013).
10. Berglund, S. P. *et al.* Photoelectrochemical oxidation of water using nanostructured $BiVO_4$ films. *J. Phys. Chem. C* **115**, 3794–3802 (2011).
11. Pilli, S. K. *et al.* Cobalt-phosphate (Co-Pi) catalyst modified Mo-doped $BiVO_4$ photoelectrodes for solar water oxidation. *Energy Environ. Sci.* **4**, 5028–5034 (2011).
12. Liang, Y. & Messinger, J. Improving $BiVO_4$ photoanodes for solar water splitting through surface passivation. *Phys. Chem. Chem. Phys.* **16**, 12014–12020 (2014).
13. Seabold, J. A. & Choi, K.-S. Efficient and stable photo-oxidation of water by a bismuth vanadate photoanode coupled with an iron oxyhydroxide oxygen evolution catalyst. *J. Am. Chem. Soc.* **134**, 2186–2192 (2012).
14. Kim, T. W. & Choi, K.-S. Nanoporous $BiVO_4$ photoanodes with dual-layer oxygen evolution catalysts for solar water splitting. *Science* **343**, 990–994 (2014).
15. McDowell, M. T. *et al.* Improved stability of polycrystalline bismuth vanadate photoanodes by use of dual-layer thin TiO_2/Ni coatings. *J. Phys. Chem. C* **118**, 19618–19624 (2014).
16. Kanan, M. W. *et al.* Structure and valency of a cobalt-phosphate water oxidation catalyst determined by *in situ* X-ray spectroscopy. *J. Am. Chem. Soc.* **132**, 13692–13701 (2010).
17. Burke, M. S., Kast, M. G., Trotochaud, L., Smith, A. M. & Boettcher, S. W. Cobalt–iron (oxy)hydroxide oxygen evolution electrocatalysts: the role of structure and composition on activity, stability, and mechanism. *J. Am. Chem. Soc.* **137**, 3638–3648 (2015).
18. Burke, M. S., Enman, L. J., Batchellor, A. S., Zou, S. & Boettcher, S. W. Oxygen evolution reaction electrocatalysis on transition metal oxides and (oxy)hydroxides: activity trends and design principles. *Chem. Mater.* **27**, 7549–7558 (2015).
19. Burke, M. S. *et al.* Revised oxygen evolution reaction activity trends for first-row transition-metal (oxy)hydroxides in alkaline media. *J. Phys. Chem. Lett.* **6**, 3737–3742 (2015).
20. Lutterman, D. A., Surendranath, Y. & Nocera, D. G. A self-healing oxygen-evolving catalyst. *J. Am. Chem. Soc.* **131**, 3838–3839 (2009).
21. Surendranath, Y., Lutterman, D. A., Liu, Y. & Nocera, D. G. Nucleation, growth, and repair of a cobalt-based oxygen evolving catalyst. *J. Am. Chem. Soc.* **134**, 6326–6336 (2012).
22. Kudo, A., Omori, K. & Kato, H. A novel aqueous process for preparation of crystal form-controlled and highly crystalline $BiVO_4$ powder from layered vanadates at room temperature and its photocatalytic and photophysical properties. *J. Am. Chem. Soc.* **121**, 11459–11467 (1999).
23. Minegishi, T., Nishimura, N., Kubota, J. & Domen, K. Photoelectrochemical properties of $LaTiO_2N$ electrodes prepared by particle transfer for sunlight-driven water splitting. *Chem. Sci.* **4**, 1120–1124 (2013).
24. Kuang, Y. *et al.* A front-illuminated nanostructured transparent $BiVO_4$ photoanode for >2% efficient water splitting. *Adv. Energy Mater.* **6**, 1501645 (2016).
25. Zhong, M. *et al.* Surface modification of CoO_x loaded $BiVO_4$ photoanodes with ultrathin *p*-type NiO layers for improved solar water oxidation. *J. Am. Chem. Soc.* **137**, 5053–5060 (2015).
26. Seabold, J. A., Zhu, K. & Neale, N. R. Efficient solar photoelectrolysis by nanoporous Mo:$BiVO_4$ through controlled electron transport. *Phys. Chem. Chem. Phys.* **16**, 1121–1131 (2013).
27. Park, Y., Kang, D. & Choi, K.-S. Marked enhancement in electron–hole separation achieved in the low bias region using electrochemically prepared Mo-doped $BiVO_4$ photoanodes. *Phys. Chem. Chem. Phys.* **16**, 1238–1246 (2014).
28. Smith, A. M., Trotochaud, L., Burke, M. S. & Boettcher, S. W. Contributions to activity enhancement via Fe incorporation in Ni-(oxy)hydroxide/borate catalysts for near-neutral pH oxygen evolution. *Chem. Commun.* **51**, 5261–5263 (2015).

29. Trotochaud, L., Young, S. L., Ranney, J. K. & Boettcher, S. W. Nickel–iron oxyhydroxide oxygen-evolution electrocatalysts: the role of intentional and incidental iron incorporation. *J. Am. Chem. Soc.* **136**, 6744–6753 (2014).
30. Friebel, D. *et al.* Identification of highly active Fe sites in (Ni,Fe)OOH for electrocatalytic water splitting. *J. Am. Chem. Soc.* **137**, 1305–1313 (2015).
31. Klaus, S., Cai, Y., Louie, M. W., Trotochaud, L. & Bell, A. T. Effects of Fe electrolyte impurities on $Ni(OH)_2$/NiOOH structure and oxygen evolution activity. *J. Phys. Chem. C* **119**, 7243–7254 (2015).
32. Kenney, M. J. *et al.* High-performance silicon photoanodes passivated with ultrathin nickel films for water oxidation. *Science* **342**, 836–840 (2013).
33. Hu, S. *et al.* Amorphous TiO_2 coatings stabilize Si, GaAs, and GaP photoanodes for efficient water oxidation. *Science* **344**, 1005–1009 (2014).
34. Sun, K. *et al.* Stable solar-driven oxidation of water by semiconducting photoanodes protected by transparent catalytic nickel oxide films. *Proc. Natl Acad. Sci. USA* **112**, 3612–3617 (2015).
35. Batchellor, A. S. & Boettcher, S. W. Pulse-electrodeposited Ni–Fe (oxy)hydroxide oxygen evolution electrocatalysts with high geometric and intrinsic activities at large mass loadings. *ACS Catalys.* **5**, 6680–6689 (2015).
36. Peter, L. M. Dynamic aspects of semiconductor photoelectrochemistry. *Chem. Rev.* **90**, 753–769 (1990).
37. Langmuir, I. The adsorption of gases on plane surfaces of glass, mica and platinum. *J. Am. Chem. Soc.* **40**, 1361–1403 (1918).
38. Jia, Q., Iwashina, K. & Kudo, A. Facile fabrication of an efficient $BiVO_4$ thin film electrode for water splitting under visible light irradiation. *Proc. Natl Acad. Sci. USA* **109**, 11564–11569 (2012).
39. Li, Y. *et al.* Cobalt phosphate-modified barium-doped tantalum nitride nanorod photoanode with 1.5% solar energy conversion efficiency. *Nat. Commun.* **4**, 2566 (2013).
40. Li, Y. *et al.* Vertically aligned Ta_3N_5 nanorod arrays for solar-driven photoelectrochemical water splitting. *Adv. Mater.* **25**, 125–131 (2013).
41. Ueda, K. *et al.* Photoelectrochemical oxidation of water using $BaTaO_2N$ photoanodes prepared by particle transfer method. *J. Am. Chem. Soc.* **137**, 2227–2230 (2015).
42. Lichterman, M. F. *et al.* Enhanced stability and activity for water oxidation in alkaline media with bismuth vanadate photoelectrodes modified with a cobalt oxide catalytic layer produced by atomic layer deposition. *J. Phys. Chem. Lett.* **4**, 4188–4191 (2013).
43. Kim, T. W. & Choi, K.-S. Improving stability and photoelectrochemical performance of $BiVO_4$ photoanodes in basic media by adding a $ZnFe_2O_4$ layer. *J. Phys. Chem. Lett.* **7**, 447–451 (2016).
44. Kim, T. W., Ping, Y., Galli, G. A. & Choi, K.-S. Simultaneous enhancements in photon absorption and charge transport of bismuth vanadate photoanodes for solar water splitting. *Nat. Commun.* **6**, 8769 (2015).
45. Saito, R., Miseki, Y. & Sayama, K. Highly efficient photoelectrochemical water splitting using a thin film photoanode of $BiVO_4/SnO_2/WO_3$ multi-composite in a carbonate electrolyte. *Chem. Commun.* **48**, 3833–3835 (2012).
46. Ding, C. *et al.* Visible light driven overall water splitting using cocatalyst/$BiVO_4$ photoanode with minimized bias. *Phys. Chem. Chem. Phys.* **15**, 4589–4595 (2013).

Acknowledgements

This work was primarily supported by the Artificial Photosynthesis Project of the Ministry of Economy, Trade and Industry (METI) of Japan. This work was also supported by a Grant-in-Aid for Specially Promoted Research (#23000009) of the Japan Society for the Promotion of Science (JSPS).

Author contributions

K.D. and A.K. conceived and directed the project. Y.K. developed the concept and carried out the experiments and data analysis. Q.J. and A.K. contributed to the synthesis of $BiVO_4$ particles. G.M. and T.M. contributed to the development of electrode fabrication method. M.N. and N.S. contributed to the STEM measurements. T.Y. and H.N. contributed to XPS measurements, data interpretation and coordinated the project. Y.K., T.Y. and T.H. wrote the manuscript. All authors reviewed the manuscript.

Additional information

Supplementary information is available for this paper.

Reprints and permissions information is available at www.nature.com/reprints.

Correspondence and requests for materials should be addressed to K.D.

How to cite this article: Kuang, Y. *et al.* Ultrastable low-bias water splitting photoanodes via photocorrosion inhibition and *in situ* catalyst regeneration. *Nat. Energy* **2**, 16191 (2016).

Competing interests

The authors declare no competing financial interests.